Check for updates

Lissajous scanning structured illumination microscopy

HYUNWOO KIM, ⓘ **YEONG-HYEON SEO,** ⓘ **JAEHUN JEON, AND KI-HUN JEONG**[*]

Department of Bio and Brain Engineering, Korea Advanced Institute of Science and Technology (KAIST) and KAIST Institute of Health Science and Technology, Daejeon 34141, South Korea
[*]*kjeong@kaist.ac.kr*

Abstract: High-resolution fluorescent microscopic imaging techniques are in high demand to observe detailed structures or dynamic mechanisms of biological samples. Structured illumination microscopy (SIM) has grabbed much attention in super-resolution imaging due to simple configuration, high compatibility with common fluorescent molecules, and fast image acquisition. Here, we report Lissajous scanning SIM (LS-SIM) by using a high fill-factor Lissajous scanning micromirror and laser beam modulation. The LS-SIM was realized by a Lissajous scanned structured illumination module, relay optics, and a conventional fluorescent microscope. The micromirror comprises an inner mirror and an outer frame, which are scanned at pseudo-resonance with electrostatic actuation. The biaxial scanning frequencies are selected by the frequency selection rule for high fill-factor (> 80%) Lissajous scanning. Structured illumination (SI) was then realized by modulating the intensity of a laser beam at the least common multiple (LCM) of the scanning frequencies. A compact Lissajous scanned SI module containing a fiber-optic collimator and Lissajous micromirror has been fully packaged and coupled with relay optics and a fiber-based diode pumped solid state (DPSS) laser including acousto-optic-modulator (AOM). Various structured images were obtained by shifting the phase and orientation of the illumination patterns and finally mounted with a conventional fluorescent microscope. The LS-SIM has experimentally demonstrated high-resolution fluorescent microscopic imaging of reference targets and human lung cancer cell PC-9 cells. The LS-SIM exhibits the observable region in spatial frequency space over 2x, the line-edge sharpness over 1.5x, and the peak-to-valley (P-V) ratio over 2x, compared to widefield fluorescent microscopy. This method can provide a new route for advanced high-resolution fluorescent microscopic imaging.

1. Introduction

Structured illumination (SI) recently serves as a leading-edge technique in advanced imaging applications such as facial recognition in mobile security [1] or motion detection and depth estimation in virtual / augmented reality [2]. Recently, structured illumination microscopy (SIM) attracts a great interest for high-resolution microscopic imaging [3–4], due to the simple working principle, high compatibility with common fluorescent molecules, and fast image acquisition [5–6]. Several patterned frames of a single target are acquired by shifting the phase and the orientation of an illumination pattern. The patterned frames are reconstructed into a single super-resolution microscopic image, which draws higher spatial frequency information in the observable region [6–7]. The SI is commonly achieved by using diffraction gratings [8–9] or spatial light modulators (SLM) such as digital micromirror device (DMD) [10–12], diffraction optical element (DOE) [13] or liquid crystal on silicon (LCOS) [14]. The diffraction gratings either require an additional component for varying structured illumination patterns or has low system flexibility for multi-wavelength structured illumination due to its varied angle of diffraction [15,16]. The SLMs finely control the illumination patterns and overcome wavelength-dependency, however, they still require high fabrication cost. Moreover, both two

methods intrinsically experience significant intensity loss of illumination patterns due to the splits of incident light and they form low contrast patterns due to incoherent LED light sources [4,10,11]. Recently, laser scanning mirrors are combined with diffraction gratings [8,17], SLMs [18], and micro-lens arrays [19] to improve the drawbacks of conventional methods. However, they still have intrinsic issues of low illumination efficiency. Besides, the addition of an extra scanner unit also increases both the complexity and the bulkiness of experimental setups. As a result, the new SI microscopic technique is still in need for not only performing highly efficient and high contrast illumination patterns but also maintaining a simple and compact experimental setup.
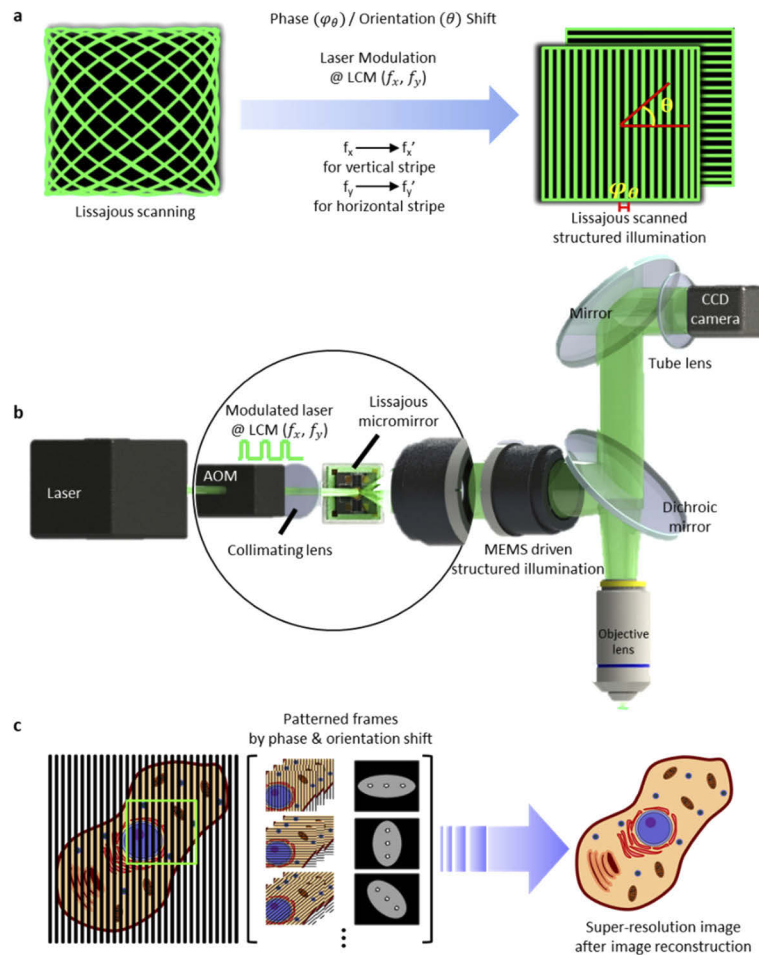
Fig. 1. Lissajous scanning structured illumination microscopy (LS-SIM). (a) Working principle of stripe illumination patterns. Lissajous scan trajectory with laser modulation at least common multiple (LCM) of biaxial scanning frequencies forms dot array illumination patterns. One axis' scanning frequency shift to the frequency in co-prime relation with non-shifted one results in phase fixation of a given axis and finally forms high contrast stripe pattern. (b) A schematic illustration of the experimental set-up for LS-SIM. (c) Patterned frames are acquired by shifting either phase or orientation of the stripe SI pattern, which causes the extension of passband in the spatial frequency domain. The LS-SIM extracts high spatial frequency information of a single target after the reconstruction of multiple patterned frames and finally creates a single resolution-enhanced image.

Laser scanning structured illumination of high efficiency and high contrast has been recently demonstrated by using high definition and high fill factor (HDHF) Lissajous scanning and laser intensity modulation [20–22]. The HDHF Lissajous microscanner based on the scanning frequency selection rule delivers high frame-rate and high mechanical stability and also has uniform illumination along with the entire field-of-view (FOV) [23,24]. The Lissajous scanned SI not only controls various illumination patterns in terms of the pattern density, the phase, and the FOV but also resolves conventional technical issues such as wavelength-dependent system flexibility issue and intensity loss owing to beam steering of scanning MEMS mirror. However, this method has not been utilized for high-resolution microscopic applications yet.

Here we report Lissajous scanning structured illumination microscopy (LS-SIM) by using laser scanning Lissajous micromirror and laser intensity modulation. The Lissajous micromirror operates at pseudo-resonance of the orthogonally disposed axes. The laser intensity is modulated at the least common multiple (LCM) of biaxial scanning frequencies to form the static illumination pattern in dot array. The biaxial scanning frequencies are determined by using the scanning frequency selection rule to acquire highly dense illumination patterns. Besides, as one axis' scanning frequency is shifted to the frequency in co-prime relation with non-shifted one, the frequency shift causes a phase fixation of the given axis and finally forms high contrast stripe illumination patterns (Fig. 1(a)). The LS-SIM comprises Lissajous micromirror, a fiber-based 532 nm diode pumped solid state (DPSS) laser with acousto-optic-modulator (AOM), fiber-optic collimator, relay optics, and a conventional fluorescent microscope (Fig. 1(b)). Various patterned frames are acquired by shifting either the phase or the orientation of illumination patterns. Resolution-enhanced microscopic images containing higher spatial frequency are obtained after the image reconstruction of multiple patterned frames (Fig. 1(c)).

2.　Results and discussion

2.1.　High fill-factor Lissajous micromirror

The Lissajous micromirror consists of two orthogonally disposed axes; an inner mirror and an outer frame, which are electrostatically tilted along with the flexure structure of each axis. The micromirror operates at pseudo-resonance where a set of biaxial scanning frequencies can be selected for HDHF Lissajous scanning [20–21]. The scanning frequency selection range was mainly controlled by the Q-factor ($= f_{resonance}/\Delta f_{FWHM}$) of Lissajous micromirror, which was theoretically calculated along with the operational damping and the spring constant of each axis' flexure [25,26]. In other words, a larger mirror diameter causes an increase in the operational damping, which finally lowers the Q-factor of Lissajous micromirror. Besides, the spring constant of flexure, proportional to the square-root of Q-factor of micromirror, is mainly determined by the Young's modulus and the structure of flexure. The spring constant of the flexure was mainly manipulated by the flexure width. The Q-factor in slow-axis, i.e., outer frame, has a relatively high Q value to avoid mechanical coupling between two orthogonally disposed axes while the Q-factor in fast-axis, i.e., inner mirror, has a low Q value to obtain a broad scanning frequency selection range for the flexible control of the pattern density.

The Lissajous micromirror was microfabricated by using a standard 6-inch silicon on insulator (SOI) process (Fig. 2(a)). The microfabrication procedure started with deep reactive ion etching (DRIE) patterning of the top Si layer. A thin silicon dioxide was thermally grown for the electrical isolation and the low pressure chemical vapor deposition (LPCVD) for poly-Si were then proceeded to fill the gaps between the electrodes. A thin gold film was thermally evaporated and defined for wire bonding and high reflection of mirror surface. The micromirror structures were defined by DRIE patterning of the top and backside Si layer. The Lissajous micromirrors were finally released through the removal of a buried oxide layer by using the buffered oxide etchant (BOE). Figure 2(b) shows the SEM image of the microfabricated Lissajous micromirror, finely defining the key operational structures such as flexure and comb-drive. The fabrication

yield was measured over 95% at a wafer level. The Q-factor was experimentally measured depending on the mirror diameter for operational damping and the flexure width for spring constant (Figs. 2(c)–2(e)). The calculated and experimental results indicate that the Q-factor is inversely proportional to the operational damping while proportional to square-root of the spring constant of flexure.
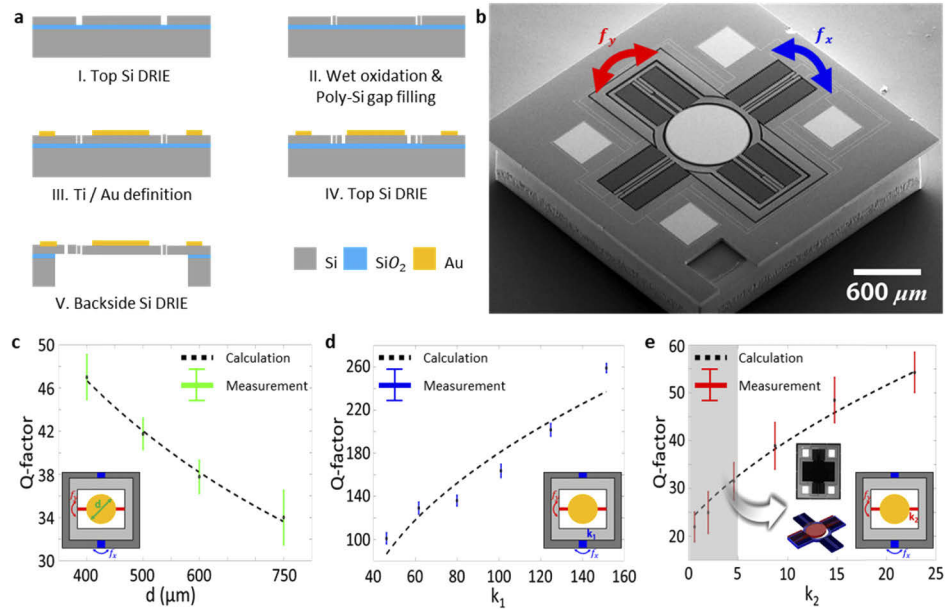
Fig. 2. Microfabrication of Lissajous micromirror and the Q-factor control parameter study. (a) The microfabrication procedure of Lissajous micromirror using a standard SOI process. (b) A SEM image of the fabricated Lissajous micromirror. The key operational structures including flexure and comb-drive are finely defined. (c-e) The Q-factor control for HDHF Lissajous scanning. Broad scanning frequency selection range is highly required for the HDHF Lissajous scanning. The Q-factor of Lissajous micromirror is manipulated depending on the operational damping by mirror diameter and the spring constant of flexure by flexure width.

An optimized Lissajous micromirror was selected based on the result of Q-factor control. The slow axis has a thick flexure width (=8 μm) to realize relatively high Q-factor. In contrast, the fast axis with a thin flexure width (=3 μm) performs a low Q-factor within the range of avoiding fracture of flexure structure due to fatigue crack or any operational instability such as coupling with undesirable higher-order operation modes. The selected Lissajous micromirror has a physical dimension of $1.7 \times 1.7 \times 0.43$ mm. The Lissajous micromirror resonates at 4,475 Hz and 6,760 Hz, respectively, showing less than 10 Hz difference from the calculated values and it has the bandwidths at full width half maximum (FWHM) of 12 Hz (Q ≈ 373) and 150 Hz (Q ≈ 45) for the outer frame and the inner mirror, respectively (Fig. 3(a)). The frame-rate and the fill-factor of Lissajous scanning were flexibly manipulated through the scanning frequency selection. In other words, the greatest common divisor (GCD) of biaxial scanning frequencies indicates the frame-rate of given Lissajous scanning. As the GCD decreases, the lobe number ($N = (f_x + f_y) / GCD(f_x, f_y)$) i.e., the number of scan lines that meets at the edge of FOV, increases and thus the fill-factor of Lissajous scanning increases (Fig. 3(b)).
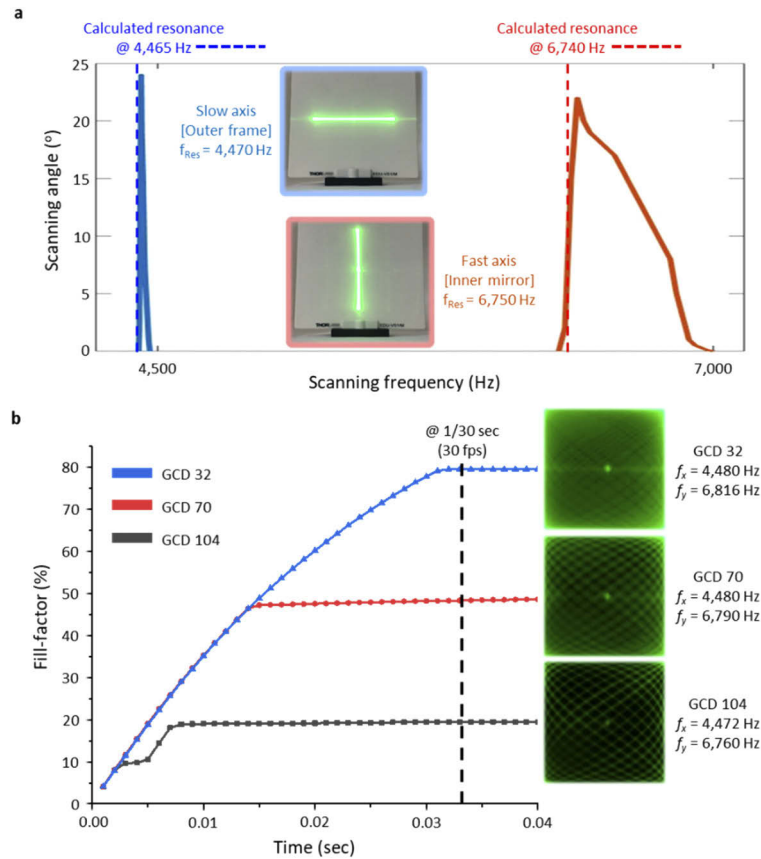
Fig. 3. Opto-mechanical properties of the selected Lissajous micromirror. (a) The scanning frequency response. The micromirror resonates at 4,475 Hz and 6,760 Hz with bandwidth of 12 Hz and 150 Hz for the outer frame and the inner mirror, respectively. (b) The frame-rate and the fill-factor of Lissajous micromirror. The greatest common divisor (GCD) of biaxial scanning frequencies indicates the frame-rate of formed Lissajous scanning. The frame-rate and the fill-factor can be flexibly controlled by the scanning frequency selection rule. Reduction in the GCD causes an increase in the lobe number N and finally, the fill-factor of the Lissajous scanning increases.
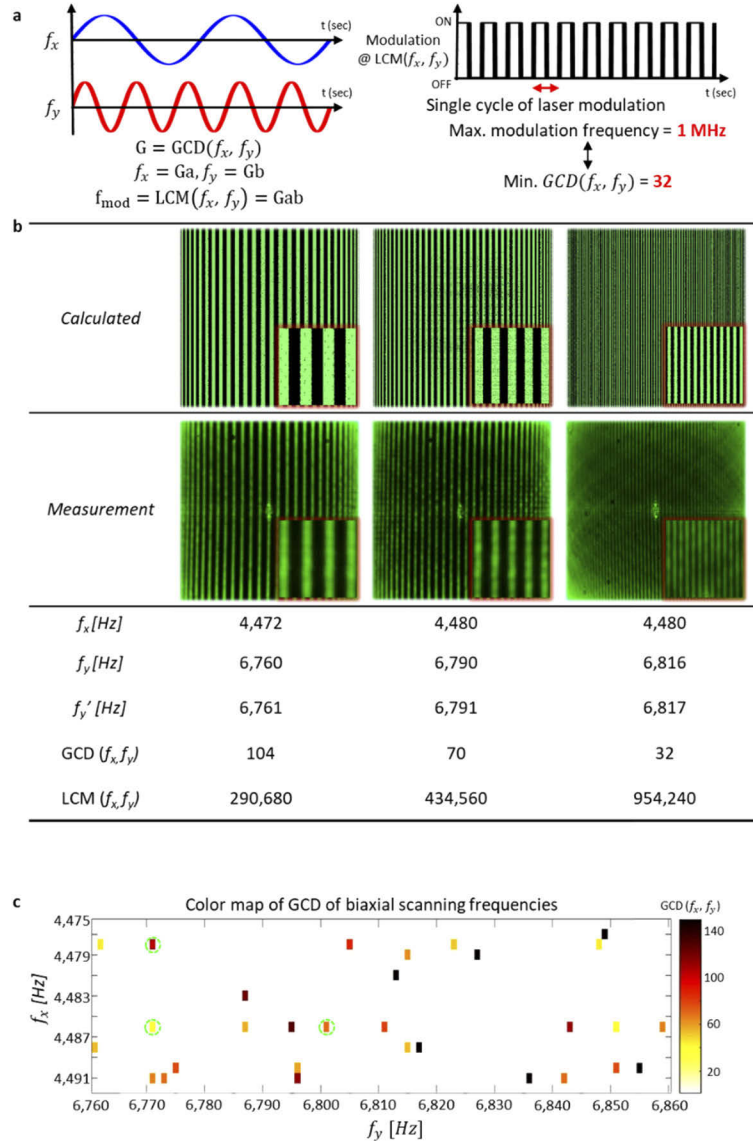
2.2. *Laser modulated structured illumination*

The illumination pattern is statically formed in dot array by modulating a laser intensity at the LCM of biaxial scanning frequencies (Fig. 4(a)). The GCD of biaxial scanning frequencies is inversely proportional to the LCM. The decrease in GCD leads to the increase in laser modulation frequency, i.e., the LCM, which forms high density Lissajous scanned SI patterns. A scanning frequency in one axis is shifted into the frequency in co-prime relation with non-shifted one and therefore the frequency shift allows a phase fixation of the given axis and finally forms a static stripe illumination pattern. In this experiment, a fiber-based 532 nm DPSS laser with AOM has the maximum modulation frequency at 1 MHz and thus the minimum GCD within the given scanning frequency selection range is limited to the GCD of 32. Arranging the frequency sets from a high GCD to low order, the fill-factor of Lissajous trajectory gradually increases. In addition, when the laser intensity modulation and the scanning frequency shift were proceeded,

the density of illumination pattern was increased along with the descending order of GCD (Fig. 4(b)).

A frequency set for LS-SIM was finally selected by a GCD color map (Fig. 4(c)). The color map shows that most frequency sets have significantly low GCD value over the entire 1,700


Fig. 4. The Lissajous scanned SI along with the GCD control. (a) The Lissajous scanned SI formation. The Lissajous micromirror operates at pseudo-resonance and the illumination pattern is statically formed by modulating a laser intensity at the LCM of biaxial scanning frequencies. (b) The Lissajous scanned SI from high GCD to low order. (1st row: simulated SI, 2nd row: captured SI) As the GCD decreases, highly dense illumination pattern is formed. The selected frequency sets are indicated from top to bottom as from coarse (high GCD) to dense (low GCD) structured illumination. (c) The GCD color map of scanning frequency sets within the operational range. Only a limited number of scanning frequency sets do not violate the minimum GCD condition.

frequency sets. For more details, only 2.41% of the entire frequency sets meets the minimum GCD condition i.e., GCD of 32 or greater (Fig. 4(d)). The statistical result indicates that a broad scanning frequency selection range by a low Q-factor design is an important factor to realize the successful LS-SIM.

A scanning module for the LS-SIM was fully packaged with the fiber-optic collimator and the PCB-bonded Lissajous micromirror disposed on 45° wedge to reflect the collimated beam into a perpendicular path through a glass window (Fig. 5(a)). The module housing has a physical dimension of $16 \times 10 \times 8.5$ mm (Fig. 5(b)).
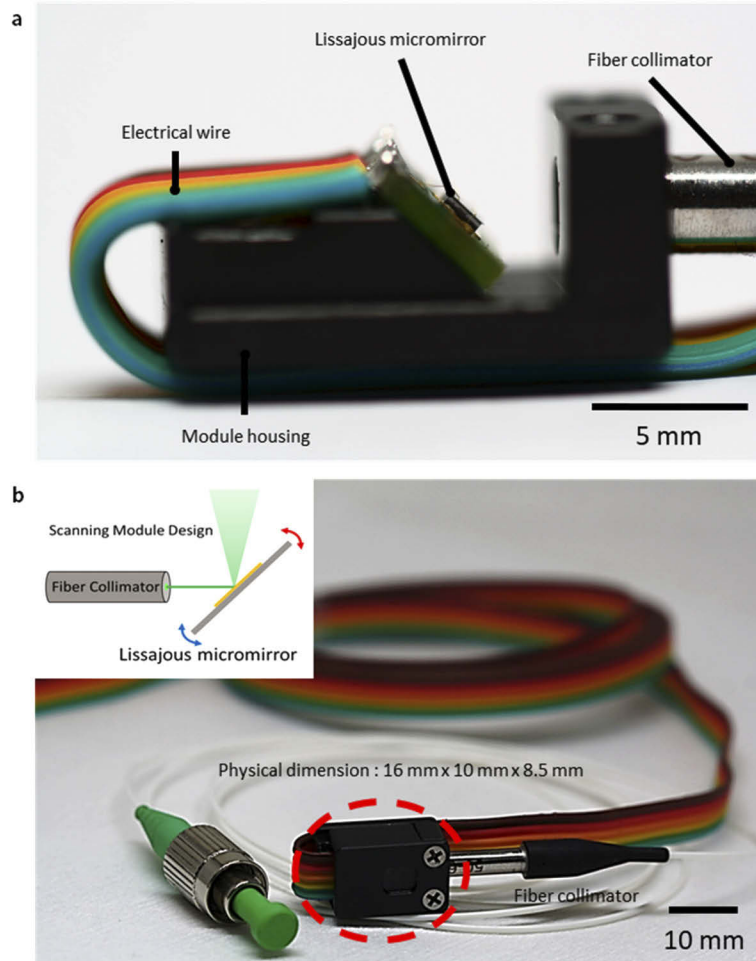

Fig. 5. A scanning module for LS-SIM. (a-b) A Lissajous scanned SI module is fully packaged with the fiber-optic collimator and the PCB wire-bonded Lissajous micromirror.

2.3. Lissajous scanning SIM (LS-SIM) for high-resolution microscopic imaging

The Lissajous scanned SI was further applied for high-resolution microscopic imaging. The fully packaged Lissajous scanned SI module was mounted with a conventional fluorescent microscope (50x objective with 0.40 NA). The resolution enhancement was characterized with a photolithographically patterned fluorescence target [27]. Various patterned frames were acquired by shifting either the phase or the orientation of illumination patterns. The reconstructed LS-SIM

images much clearly define the details of target sample than the conventional microscopic images (Figs. 6(a) and 6(d)). Supporting details in terms of the observable region in the Fourier magnitude spectrum, the line-edge sharpness and the peak-to-valley (P-V) ratio were additionally analyzed (Figs. 6(b), 6(c), and 6(e)). In details, the observable region in the Fourier magnitude spectrum is extended over 2x with the LS-SIM, which acquires higher spatial frequency information of the target. Besides, the line-edge sharpness and the P-V ratio are also measured from the intensity profile along with the dotted lines of a-a' and b-b' in Figs. 6(a) and 6(d), respectively. Dashed lines in Fig. 6(c) are data points for 90% (blue) and 10% (green) of intensity for 10-90% rise of each data set, respectively. As a result, the line-edge sharpness is enhanced over 1.5x while the P-V ratio is enhanced over 2x, respectively, compared to widefield fluorescent microscopy.
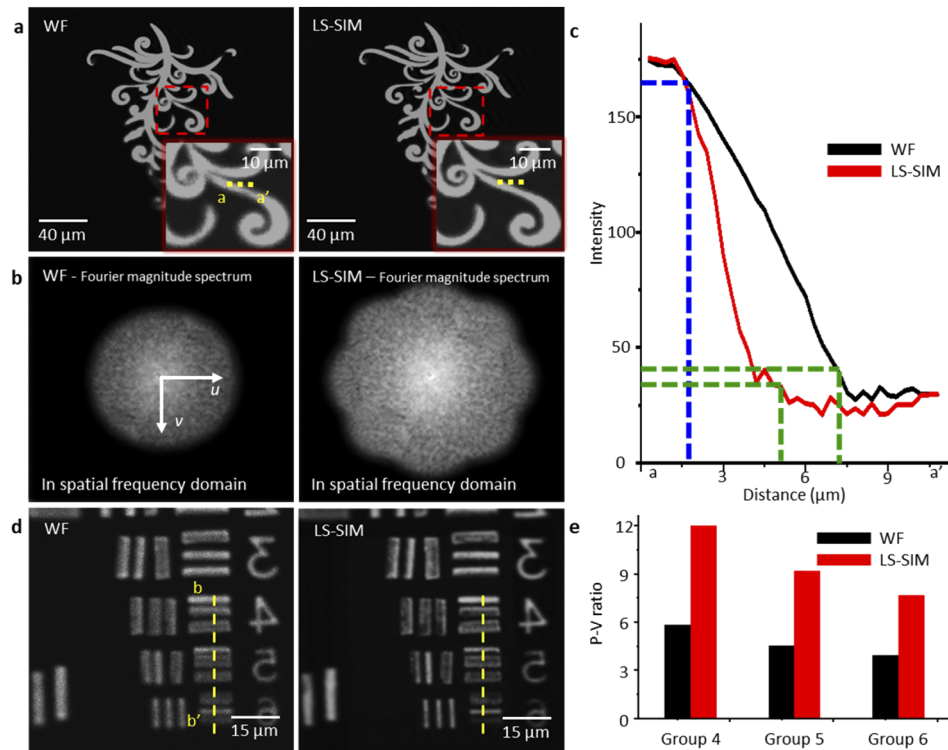
Fig. 6. Microscopic fluorescent images through LS-SIM and a comparison between the conventional fluorescent microscopy and the LS-SIM. (a,d) Reference fluorescent target imaging to prove resolution enhancement of the LS-SIM. (b,c,e) The Fourier magnitude spectrum, the line-edge sharpness, and the P-V ratio are acquired for additional supporting analysis. (WF: Widefield fluorescent microscopy, LS-SIM: Lissajous scanning SIM)

The LS-SIM has also experimentally demonstrated high-resolution cellular imaging (Fig. 7). The cellular imaging of human lung cancer cell PC-9 cells was compared by widefield (WF) fluorescent microscopy, confocal laser scanning microscopy (CLSM), and LS-SIM (Figs. 7(a)–7(b)). Both the CLSM and the LS-SIM images finely define the fluorescent signals, whereas the WF image shows blurred fluorescent signals along with the cellular membrane. In particular, the line-edge sharpness of LS-SIM is enhanced over 1.3x compared to the case of CLSM. In addition, various fluorescent dyes were stained to prove high compatibility with common fluorescent dyes. The captured fluorescent images show that individual fluorescent signals are clearly captured in the reconstructed LS-SIM image and therefore the LS-SIM provides a substantial image resolution-enhancement compared to the WF microscope (Figs. 7(c)–7(d)).
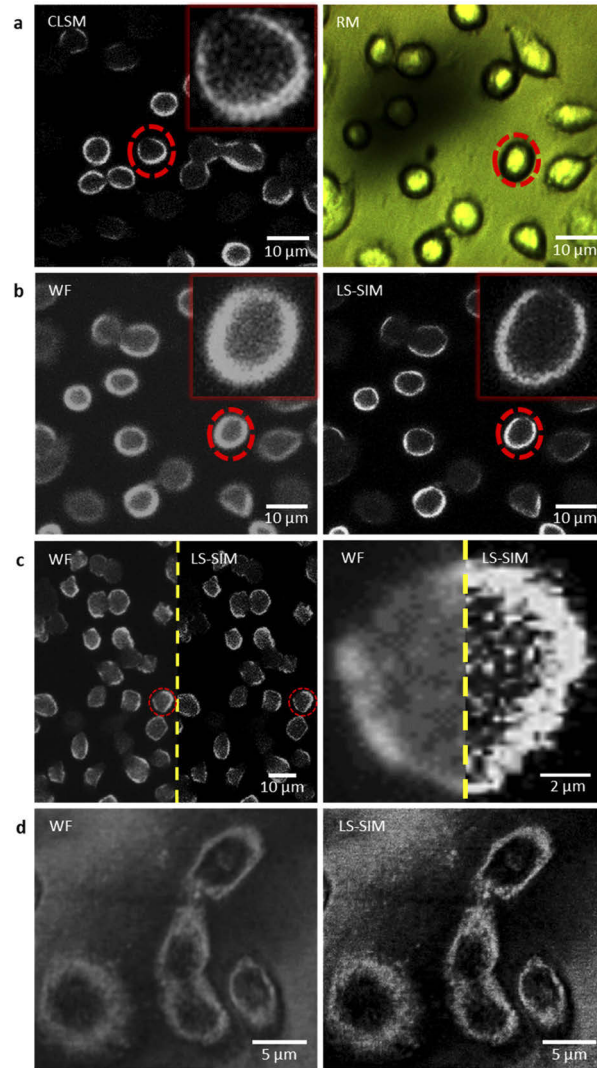
Fig. 7. The LS-SIM in the cellular imaging application. (a-b) The LS-SIM has been demonstrated with human lung cancer cell PC-9 cells. Various fluorescent dyes such as PI dye and cytoskeleton fluorescent dye, are used to prove high compatibility with common fluorescent dyes. The reconstructed LS-SIM images experience a significant resolution enhancement. (RM: Reflectance microscopy, WF: Widefield fluorescent microscopy, CLSM: Confocal laser scanning microscopy, LS-SIM: Lissajous scanning SIM)

3. Conclusion

In this work, the Lissajous scanning SIM has been successfully demonstrated by the Lissajous scanning micromirror with a laser intensity modulation. The micromirror comprises a low Q-factor inner mirror to allow a broad selection range of scanning frequencies and a relatively high Q-factor outer frame to reduce the mechanical coupling between two orthogonally disposed axes. A high fill-factor Lissajous scanning was achieved by using the scanning frequency selection and the Lissajous scanned SI was finally realized by modulating a laser intensity at the LCM of biaxial scanning frequencies. The LS-SIM demonstrates high-resolution fluorescent imaging after the image reconstruction of multiple patterned frames. The resolution enhancement of LS-SIM was experimentally confirmed in terms of the Fourier magnitude spectrum, the line-edge sharpness, and the P-V ratio. Finally, the LS-SIM has been further applied to cancer cell imaging with high contrast individual fluorescent signals. Further improvement of the LS-SIM can be achieved by defining non-linearity from the SI pattern shifts and optimizing the image reconstruction algorithm. The Lissajous scanning SIM can provide a new perspective for high-resolution fluorescent microscopic applications due to high system flexibility, wavelength insensitiveness, and high illumination efficiency.

Funding

Disclosures

The authors declare no competing financial interests.

References

1. J. Yang and H. Chen, The 3D reconstruction of face model with active structured light and stereo vision fusion, *3rd IEEE International Conference on Computer and Communications (ICCC)*, pp. 1902–1906 (2017)
2. H. M. Hondori, M. Khademi, L. Dodakian, S. C. Cramer, and C. V. Lopes, "A Spatial Augmented Reality rehab system for post-stroke hand rehabilitation," Stud. Health Technol. Inform **184**, 279–285 (2013).
3. D. Li, L. Shao, B.-C. Chen, X. Zhang, M. Zhang, B. Moses, D. E. Milkie, J. R. Beach, J. A. H. Ill, M. Pasham, T. Kirchhausen, M. A. Baird, M. W. Davidson, P. Xu, and E. Betzig, "Extended-resolution structured illumination imaging of endocytic and cytoskeletal dynamics," Science **349**(6251), aab3500 (2015).
4. M. Saxena, G. Eluru, and S. S. Gorthi, "Structured illumination microscopy," Adv. Opt. Photonics **7**(2), 241–275 (2015).
5. F. Ströhl and C. F. Kaminski, "Frontiers in structured illumination microscopy," Optica **3**(6), 667–677 (2016).
6. Y. Wu and H. Shroff, "Faster, sharper, and deeper: structured illumination microscopy for biological imaging," Nat. Methods **15**(12), 1011–1019 (2018).
7. A. Lal, C. Shan, and P. Xi, "Structured illumination microscopy image reconstruction algorithm," IEEE J. Sel. Top. Quantum Electron. **22**(4), 50–63 (2016).
8. Z. Li, J. Hou, J. Suo, C. Qiao, L. Kong, and Q. Dai, "Contrast and resolution enhanced optical sectioning in scattering tissue using line-scanning two-photon structured illumination microscopy," Opt. Express **25**(25), 32010–32020 (2017).
9. Y. Hirano, A. Matsuda, and Y. Hiraoka, "Recent advancements in structured-illumination microscopy toward live-cell imaging," Microscopy **64**(4), 237–249 (2015).
10. X. Zhou, M. Lei, D. Dan, B. Yao, Y. Yang, J. Qian, G. Chen, and P. R. Bianco, "Image recombination transform algorithm for superresolution structured illumination microscopy," J. Biomed. Opt. **21**(9), 096009 (2016).
11. F. Gao, H. Muhamedsalih, and X. Jiang, "Surface and thickness measurements of transparent thin-film layers utilizing modulation-based structured-illumination microscopy," Opt. Express **26**(3), 2944–2953 (2018).
12. N. Chakrova, R. Heintzmann, B. Rieger, and S. Stallinga, "Studying different illumination patterns for resolution improvement in fluorescence microscopy," Opt. Express **23**(24), 31367–31383 (2015).
13. S.-P. Yang, J.-B. Kim, Y.-H. Seo, and K.-H. Jeong, "Rotational Offset Microlens Arrays for Highly Efficient Structured Pattern Projection," Adv. Opt. Mater. **8**(16), 2000395 (2020).
14. P. Křížek, I. Raška, and G. M. Hagen, "Flexible structured illumination microscope with a programmable illumination array," Opt. Express **20**(22), 24585–24599 (2012).

15. M. G. L. Gustafsson, L. Shao, P. M. Carlton, C. J. R. Wang, I. N. Golubovskaya, W. Z. Cande, D. A. Agard, and J. W. Sedat, "Three-dimensional Resolution Doubling in Wide-field Fluorescence Microscopy by Structured Illumination," Biophys. J. **94**(12), 4957–4970 (2008).

16. R. Förster, H.-W. Lu-Walther, A. Jost, M. Kielhorn, K. Wicker, and R. Heinyzmann, "Simple structured illumination microscope setup with high acquisition speed by using a spatial light modulator," Opt. Express **22**(17), 20663–20677 (2014).

17. O. Mandula, M. Kielhorn, K. Wicker, G. Krampert, I. Kleppe, and R. Heintzmann, "Line scan-structured illumination microscopy super-resolution imaging in thick fluorescent samples," Opt. Express **20**(22), 24167–24174 (2012).

18. Y. Huang, D. Zhu, L. Jin, C. Kuang, Y. Xu, and X. Liu, "Laser scanning saturated structured illumination microscopy based on phase modulation," Opt. Commun. **396**, 261–266 (2017).

19. A. G. York, P. Chandris, D. D. Nogare, J. Head, P. Wawrzusin, R. S. Fischer, A. Chitnis, and H. Shroff, "Instant super-resolution imaging in live cells and embryos via analog image processing," Nat. Methods **10**(11), 1122–1126 (2013).

20. K. Hwang, Y.-H. Seo, J. Ahn, P. Kim, and K.-H. Jeong, "Frequency selection rule for high definition and high frame rate Lissajous scanning," Sci. Rep. **7**(1), 14075 (2017).

21. Y.-H. Seo, K. Hwang, H. Kim, and K.-H. Jeong, "Scanning MEMS Mirror for High Definition and High Frame Rate Lissajous Patterns," Micromachines **10**(1), 67 (2019).

22. Y.-H. Seo, H. Kim, S.-P. Yang, K. Hwang, and K.-H. Jeong, "Lissajous scanned variable structured illumination for dynamic stereo depth map," Opt. Express **28**(10), 15173–15180 (2020).

23. K. Hwang, Y.-H. Seo, and K.-H. Jeong, "Microscanners for optical endomicroscopic applications," Micro and Nano Syst. Lett. **5**(1), 1 (2017).

24. W. Liang, K. Murari, Y. Zhang, Y. Chen, M. -J. Li, and X. Li, "Increased Illumination Uniformity and Reduced Photodamage Offered by the Lissajous Scanning in Fiber-Optic Two-Photon Endomicroscopy," J. Biomed. Opt. **17**(2), 021108 (2012).

25. R. Farrugia, B. Portelli, I. Grech, D. Camilleri, O. Casha, J. Micallef, and E. Gatt, "Air Damping Analysis in Resonating Micro-Mirrors," *Symposium on Design, Test, Integration & Packaging of MEMS and MOEMS (DTIP)*, pp. 1–5 (2018).

26. T. Izawa, T. Sasaki, and K. Hane, "Scanning Micro-Mirror with an Electrostatic Spring for Compensation of Hard-Spring Nonlinearity," Micromachines **8**(8), 240 (2017).

27. D. Keum, H. Jung, and K.-H. Jeong, "Planar Emulation of Natural Compound Eyes," Small **8**(14), 2169–2173 (2012).